# Photoinduced dynamics of a quasicrystalline excitonic insulator

Ken Inayoshi ●,* Yuta Murakami ●, and Akihisa Koga ●

*Department of Physics, Tokyo Institute of Technology, Meguro, Tokyo 152-8551, Japan*

We study the photoinduced dynamics of the excitonic insulator in the two-orbital Hubbard model on the Penrose tiling by means of the time-dependent real-space mean-field approximation. We show that, with a single-cycle electric-field pulse, the bulk (spatially averaged) excitonic order parameter decreases in the Bardeen-Cooper-Schrieffer (BCS) regime, while it increases in the Bose-Einstein condensate (BEC) regime. This behavior is in common with the excitonic insulator in the square lattice reported previously. To explore the dynamics peculiar to the Penrose tiling, we examine the coordination number dependence of observables and analyze the perpendicular space. In the BEC regime, characteristic oscillations of the electron number at each site are induced by the pulse, which are not observed in normal crystals with single coordination number. On the other hand, the dynamics in the BCS regime is characterized by drastic change in the spatial pattern of the excitonic order parameter. Our results imply that potentially interesting nonequilibrium physics is caused by rich local structural patterns involved in quasicrystals.

## I. INTRODUCTION

Quasicrystals (QCs) are characterized by a long-range order without translational symmetry. Experimental and theoretical efforts have been done to clarify physical properties inherent in the QCs since its discovery in 1984 [1,2]. Recently the scope of this field has been extended due to reports of new quasicrystalline or approximant materials. One of the important examples is the superconductivity observed in Al-Zn-Mg quasicrystalline alloy [3], which exemplifies the existence of ordered phases and pair condensation even in QCs. Another important example is semiconducting behavior in the approximant Al-Si-Ru [4], which indicates the possibility of semiconducting QCs and brings attention to the physics close to the metal-insulator transition in QCs.

Despite of these efforts in research of QC, most of previous studies have mainly focused on static properties such as transport and specific heat to characterize QC [5–14]. Their nonequilibrium properties have only been studied in limited setups [15,16] and are not well understood, in contrast to those for the crystals. In normal crystals, the effect of photoexcitations has been discussed [17–23], and novel properties have been clarified such as nonthermal superconductivity [24–27] and charge density orders [28–33]. When dynamical properties are analyzed in normal crystals, relevant physics is often discussed *in the momentum space*. On the other hand, in QCs, the momentum space is not well defined due to the lack of the translational symmetry and such a discussion is not directly applicable. Thus, a simple but important question arises: how is the nonequilibrium (in particular photoinduced) dynamics in QCs similar to or different from that in normal crystals? One can also expect that a characteristic spatial dynamics

is induced by photoexcitations in QCs reflecting their lattice structure.

In order to answer the fundamental question for nonequilibrium dynamics in QCs, we focus on the excitonic insulating (EI) phase, which is known as the macroscopic quantum condensed state of electron-hole pairs (excitons) in semimetals and semiconductors [34,35]. We choose the EI phase because its nonequilibrium dynamics is recently actively studied for normal crystals and this phase should be conceptually relevant to the recently-reported semiconducting approximant Al-Si-Ru and the superconducting QC Al-Zn-Mg. In normal crystals, the research of the EI state has been boosted due to recent proposals of candidate materials such as $Ta_2NiSe_5$ [36,37] and $1T$-TiSe$_2$ [38,39]. Effects of strong photoexcitations on these materials have been experimentally investigated, where the enhancement [40], robustness [41] or suppression [42–45] of the order have been reported depending on the excitation conditions. These experiments stimulate further theoretical studies on nonequilibrium phenomena in the EI phase [46–56]. In particular, it has been recently shown that the photoinduced dynamics in the EI phase is qualitatively different in the Bardeen-Cooper-Schrieffer (BCS) and Bose-Einstein condensate (BEC) regimes, which can be explained by the dynamics of the order parameters in the momentum space [48,53].

In this paper, in light of these situations, we study the photoinduced dynamics of the EI state on a QC, considering the setup similar to that for the square lattice [48]. Namely, we deal with the two-orbital Hubbard model on the Penrose tiling [57], which is a prototypical theoretical model of the QCs, see Fig. 1. In our previous study [58], we have explored the equilibrium EI state on this model and found the characteristic condensation. In this paper, we extend the previous work to nonequilibrium systems and study the model by means of the time-dependent
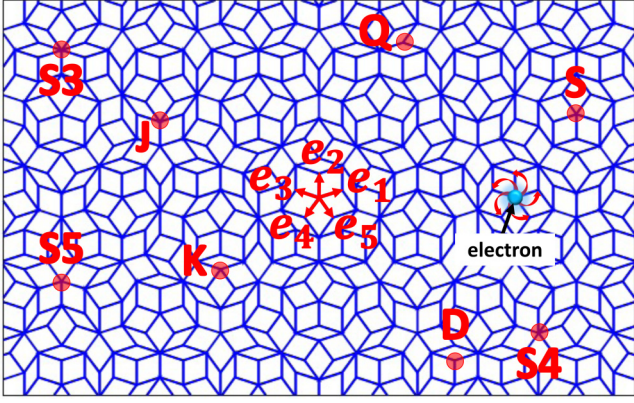
FIG. 1. Vertex model on the Penrose tiling and eight types of vertices. $e_1, \ldots, e_5$ are projection of the translational vectors in five dimensions, $\mathbf{n} = (n_1, n_2, n_3, n_4, n_5) = (1, 0, 0, 0, 0), \ldots, (0, 0, 0, 0, 1)$. Using the integers $\{n_i\}$, the lattice point $\boldsymbol{r}$ is represented as $\boldsymbol{r} = \sum_i n_i e_i$.

real-space mean-field (Hartree-Fock) approximation. We clarify that the photoirradiation decreases (increases) the bulk average of the EI order parameter in the BCS (BEC) regime, which phenomena are similar to that in the Hubbard model on the square lattice [48]. To explore the characteristic dynamics on the Penrose tiling, we examine the coordination number dependence of observables. It is found that charge fluctuations are enhanced in the BEC regime, which have not been observed in the conventional periodic systems. We also analyze the dynamics in the perpendicular space, which allows us to systematically discuss how the local environments affect local physical quantities. It is found that the spatial pattern of the EI order parameter changes remarkably in the BCS regime. This paper is organized as follows. In Sec. II, we introduce the two-orbital Hubbard model on the Penrose tiling and our numerical technique. In Sec. III, we show the results of numerical simulations. In Sec. III A, we explain the EI state in equilibrium. In Sec. III B, we study the time-evolution of the system triggered by the single-cycle pulse to explore the dynamics peculiar to the Penrose tiling. Summary and outlook are given in the last section.

## II. MODEL AND METHOD

In this paper, we consider the two-orbital Hubbard model to discuss the EI state at zero temperature. The Hamiltonian is expressed as

$$
\begin{aligned}
\hat{H} = &-J \sum_{\langle i,j \rangle \sigma} (\hat{c}_{i\sigma}^\dagger \hat{c}_{j\sigma} - \hat{f}_{i\sigma}^\dagger \hat{f}_{j\sigma}) + \frac{D}{2} \sum_{i\sigma} (\hat{n}_{ci\sigma} - \hat{n}_{fi\sigma}) \\
&- \mu \sum_{i\sigma} (\hat{n}_{fi\sigma} + \hat{n}_{ci\sigma}) + U \sum_i (\hat{n}_{ci\uparrow} \hat{n}_{ci\downarrow} + \hat{n}_{fi\uparrow} \hat{n}_{fi\downarrow}) \\
&+ V \sum_{i\sigma\sigma'} \hat{n}_{ci\sigma} \hat{n}_{fi\sigma'}, \quad (1)
\end{aligned}
$$

where $\hat{f}_{i\sigma}^\dagger$ ($\hat{c}_{i\sigma}^\dagger$) is a creation operator of the electron at site $i$ with spin $\sigma \in \{\uparrow, \downarrow\}$ in the $f$ orbital ($c$ orbital), $\hat{n}_{ci\sigma} = \hat{c}_{i\sigma}^\dagger \hat{c}_{i\sigma}$ and $\hat{n}_{fi\sigma} = \hat{f}_{i\sigma}^\dagger \hat{f}_{i\sigma}$. $J$ ($-J$) is the hopping integral between the

nearest-neighbor sites in the $f$ orbital ($c$ orbital), $D$ is the energy difference between two bands, and $\mu$ is the chemical potential. $U(>0)$ is the intraorbital on-site interaction and $V(>0)$ is the interorbital on-site interaction. In the following, we consider the half-filling condition, i.e., $\mu = U/2 + V$.

In this paper, we treat the Penrose tiling as one of examples in quasiperiodic lattices. It is composed of the fat and skinny rhombuses and includes eight kinds of vertices [59,60], whose coordination number (the number of bonds) takes 3 to 7, as shown in Fig. 1. Here, we consider the vertex model [61], where electrons are located at vertices and hop along edges of rhombuses. We set the length of edge to 1.

To discuss photoinduced dynamics of the two-orbital Hubbard model on the Penrose tiling, we introduce the dipole transition term between two bands. The corresponding Hamiltonian [48,53] is represented as

$$
\hat{H}_{\text{ex}}(t) = F_{\text{ex}}(t) \sum_{i\sigma} (\hat{c}_{i\sigma}^\dagger \hat{f}_{i\sigma} + \text{H.c.}), \quad (2)
$$

where $F_{\text{ex}}(t) = F_0 \sin(\omega t)\theta(t)\theta(t_p - t)$ expresses the time-dependent external electric field. $\theta(t)$ is the Heaviside step function, $|F_0|$ is the magnitude of the external field, $\omega$ is the frequency, and $t_p$ is the light irradiation time. Although, in more realistic and general setups, we also need to treat the intraband excitations, in this paper, we consider only the interband transitions to keep the problem simple and imitate the setup of the previous work for a normal crystal (the square lattice) [48].

To study the nonequilibrium dynamics, we employ the time-dependent real-space mean-field (MF) approximation. This enables us to treat the large system size, which is important to discuss the effects of quasiperiodic structures and electric properties inherent in the Penrose tiling [58,62–66]. While the MF theory can capture the large system, we note that the time-dependent MF theory should be reliable for simulating short-time dynamics but cannot handle long-time dynamics involving the thermalization. Actually, this scope of application of MF theory is confirmed in several previous studies [51,55,67], where the MF theory and more sophisticated theories (e.g., the nonequilibrium Green's function method) are compared in normal crystals. Strictly speaking, also in the study of QCs, it is necessary to compare the sophisticated theories and the MF theory as well to define the scope of the application. However, this comparison is difficult at the present because the sophisticated methods have large computational cost in large-size systems, and small-size systems cannot fully capture effects peculiar to QCs. In the future, when sophisticated methods that can handle the dynamics in large nonuniform systems are developed, comparison between those sophisticated methods and the MF method is important and necessary.

In the MF theory, we use the site-dependent MF parameters that are represented by means of the wave function $|\psi(t)\rangle$ as

$$
n_{fi}(t) = \langle \psi(t) | \hat{f}_{i\sigma}^\dagger \hat{f}_{i\sigma} | \psi(t) \rangle, \quad (3)
$$

$$
n_{ci}(t) = \langle \psi(t) | \hat{c}_{i\sigma}^\dagger \hat{c}_{i\sigma} | \psi(t) \rangle, \quad (4)
$$

$$
\Delta_i(t) = \langle \psi(t) | \hat{c}_{i\sigma}^\dagger \hat{f}_{i\sigma} | \psi(t) \rangle. \quad (5)
$$

Here, $n_{fi}(t)$ and $n_{ci}(t)$ are the electron numbers in $f$ and $c$ orbitals, and $\Delta_i(t)$ is the order parameter of the EI state at site $i$. Here, our discussions are restricted to the paramagnetic case, where the spin indices are omitted. Strictly speaking, one needs to consider the possibility of other orders, such as charge orders and magnetic orders, to determine the rigorous phase diagram in equilibrium. However, since the goal of this paper is to clarify the effects of quasiperiodic lattices on dynamics, we focus on the EI phase as in the previous paper for the square lattice [48] and use the above sets of MF parameters. The explicit form of the MF Hamiltonian is

$$
\begin{aligned}
\hat{H}_{\mathrm{MF}}^{\mathrm{total}}(t) = {} & J \sum_{\langle i,j \rangle} (\hat{f}_i^\dagger \hat{f}_j - \hat{c}_i^\dagger \hat{c}_j) + \frac{D}{2} \sum_i (\hat{n}_{ci} - \hat{n}_{fi}) + (2V - U) \\
& \times \sum_i \left[ \left\{ n_{ci}(t) - \frac{1}{2} \right\} \hat{n}_{fi} + \left\{ n_{fi}(t) - \frac{1}{2} \right\} \hat{n}_{ci} \right] \\
& - \sum_i [\{V \Delta_i(t) - F_{\mathrm{ex}}(t)\} \hat{f}_i^\dagger \hat{c}_i + \mathrm{H.c.}].
\end{aligned} \tag{6}
$$

Detailed derivation of Eq. (6) is given in Appendix A. Then, the time evolution of the ground state is expressed as

$$
|\psi(t)\rangle = T_t \exp\left[ -\frac{i}{\hbar} \int_0^t \hat{H}_{\mathrm{MF}}^{\mathrm{total}}(t') dt' \right] |\psi(0)\rangle, \tag{7}
$$

where $T_t$ is the time-ordering operator and $|\psi(0)\rangle$ is the ground state of $\hat{H}_{\mathrm{MF}}^{\mathrm{total}}(t=0)$.

If one examines the time evolution of the mean fields, it is not necessary to calculate the wave function (7). Instead, we evaluate the evolution of the single-particle density matrix defined as

$$
\rho_{ia,jb}(t) = \langle \psi(t) | \hat{b}_j^\dagger \hat{a}_i | \psi(t) \rangle, \tag{8}
$$

where $\hat{a}_i^\dagger$ is a creation operator of the electron at site $i$ and $a(= c, f)$ orbital. Then, the time evolution of $\boldsymbol{\rho}(t)$ is given by

$$
i\hbar \frac{\partial}{\partial t} \boldsymbol{\rho}(t) = [\boldsymbol{H}^{\mathrm{MF}}(t), \boldsymbol{\rho}(t)]. \tag{9}
$$

Here, $\boldsymbol{H}^{\mathrm{MF}}(t)$ ($\boldsymbol{\rho}(t)$) is the matrix with elements $H_{ia,jb}^{\mathrm{MF}}(t)$ ($\rho_{ia,jb}(t)$), and $H_{ia,jb}^{\mathrm{MF}}(t)$ is the matrix element of the MF Hamiltonian (6) defined as $\hat{H}_{\mathrm{MF}}^{\mathrm{total}}(t) = \sum_{ia,jb} H_{ia,jb}^{\mathrm{MF}}(t) \hat{a}_i^\dagger \hat{b}_j$. Since $\boldsymbol{H}^{\mathrm{MF}}(t)$ is a function of $\boldsymbol{\rho}(t)$, we can numerically solve Eq. (9). Here, we use the fourth-order Runge-Kutta method with the time slice $\Delta t = 0.1\hbar/J$, where the numerical error is negligible in our simulation with $t < 100\hbar/J$.

When no external field is applied, the electron number at site $i$ in the $a$ orbital is represented as

$$
\begin{aligned}
\frac{\partial}{\partial t} n_{ai}(t) &= \frac{\partial}{\partial t} \rho_{ia,ia}(t) \\
&= -\frac{J^a}{i\hbar} \left\{ \sum_m \rho_{ia,ma}(t) - \sum_m \rho_{ma,ia}(t) \right\}, \tag{10}
\end{aligned}
$$

where $m$ runs the nearest neighbor sites for site $i$ and $J^c = -J$, $J^f = J$. Then, we obtain

$$
\frac{\partial}{\partial t} \overline{n_a(t)} = 0, \tag{11}
$$

where $\overline{n_a(t)} = \sum_i n_{ai}(t)/N$ and $N$ is the number of sites. This is a natural consequence from the fact that the Hamiltonian conserves the number of electrons in each orbital without the electric field. Equation (11) is useful to check the numerical accuracy in our simulations.

In the following, we take $J$ as the unit of the energy and set $\hbar = 1$. Thus, the units of time and frequency are $\hbar/J = 1$ and $J/\hbar = 1$, respectively. We treat the two-orbital Hubbard model with $U = D = 4$. The Penrose tiling is generated in terms of the deflation rule [57]. We mainly treat the large cluster with the total sites $N = 11006$ under the open boundary condition to discuss the real-time dynamics in the quasiperiodic system. The finite size effect will be discussed in the Appendix C.

## III. RESULTS

### A. Equilibrium

Before starting with discussion of the nonequilibrium dynamics, we explain the EI state in equilibrium. At the first, we comment about the excitonic condensation in the QC. The concept of excitons is well defined even without the momentum space. It can be regarded as the bound state of an electron and a hole added to the normal semiconducting state, which is the two-body problem interacting with attractive interaction on the Penrose tiling. Without the momentum space, we can define the energy "band" and energy gap (single-particle excitation gap) between bands by looking at the eigenenergies of the single-particle states of the Hamiltonian $\hat{H}_{\mathrm{MF}}(0)$. Therefore, we can understand that the excitonic condensation occurs when the exciton binding energy is larger than the excitation gap. Of course, we can understand this condensation as a spontaneous symmetry breaking. Our model Hamiltonian $\hat{H}$ [Eq. (1)] has the U(1) symmetry since the number of $c-$ and $f-$orbital electrons are conserved ($[\hat{H}, \sum_i \hat{c}_i^\dagger \hat{c}_i] = [\hat{H}, \sum_i \hat{f}_i^\dagger \hat{f}_i] = 0$). When the EI order is realized with nonzero $\Delta_i$, this symmetry is broken. This situation is same as in the theoretical studies of superconductor on the Penrose tiling [62]. Note that in general and realistic systems [68–70], the Hamiltonian has some discrete symmetry instead of U(1) symmetry. The detailed study will be discussed elsewhere.

Figure 2 shows the spatially-averaged EI order parameter $\overline{\Delta}$ and single-particle gap $\Delta_{\mathrm{Gap}}$ as a function of the interorbital interaction $V$, where $\overline{\Delta} = \sum_{i=1}^N \Delta_i(0)/N$ and we take $\Delta_i(0)$ as the positive value. $\Delta_{\mathrm{Gap}}$ is defined as the difference between the minimum energy of the unoccupied single-particle states and the maximum energy of the occupied single-particle states of $\hat{H}_{\mathrm{MF}}^{\mathrm{total}}(t=0)$. When $V = 0$, the system is metallic since the level difference $D$ is smaller than the bandwidth $W$. Introducing $V$, the EI order is induced with the finite order parameter $\overline{\Delta}$ and the gap $\Delta_{\mathrm{gap}}$ opens around the Fermi level, as shown in Fig. 2. Increasing the interaction, $\overline{\Delta}$ and $\Delta_{\mathrm{gap}}$ increase, have a maximum, and decrease. At $V = V_c$, the order parameter $\overline{\Delta}$ vanishes, and the quantum phase transition occurs to the band insulating (BI) state. It is well known that, in the EI state with $0 < V < V_c$, the spatial extent of electron-hole pair is larger in the weak coupling regime ($V \sim 0$), while is smaller in the strong coupling regime ($V \sim V_C$). These are characterized by the BCS and BEC regimes, respectively.
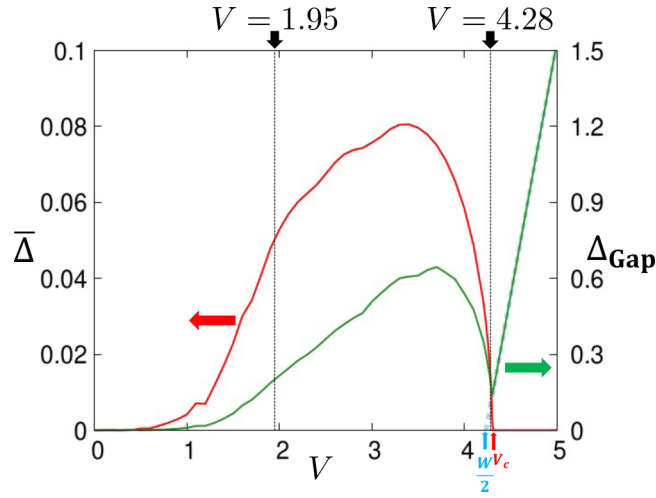
FIG. 2. $\overline{\Delta}$ and $\Delta_{\text{Gap}}$ in the system with $U = D = 4$ and $N = 11\,006$. The excitation gap in the BI state is given by $2V - W$, which is shown with the light-blue dashed line. Here, $W$ ($\simeq 8.4$) is the bandwidth of the vertex model. We define the bandwidth as the difference between the maximum and minimum energy eigenvalues of the tight-binding model at $U = D = V = 0$.

Note that the boundary of the BCS and BEC regimes is not well defined (it is a crossover) and conventionally there are several criterions to determine the crossover regime. In this paper, we decided to use the maximum point of the EI order ($V \sim 3.35$) as the boundary [48,52]. The difference of the spatial extent of electron-hole pairs should be confirmed in the off-site electron-hole pair amplitude $OP(r_{ij}) = \langle \psi(0)|\hat{c}_i^\dagger \hat{f}_j|\psi(0)\rangle$, where $r_{ij}$ is a distance between sites $i$ and $j$. Figure 3 shows that the pair amplitude in the BEC regime decays faster than that in the BCS regime. This means that, in the BCS regime, the electron-hole pairs are spatially extended, while in the BEC regime, they are confined, as discussed above. In the paper, we mainly focus on the cases with the interorbital interactions $V = 1.95$ and $4.28$ as examples of the

BCS and BEC states, where the single-particle gap is the same ($\Delta_{\text{gap}} = 0.2$).

In Fig. 4, we show the density of states (DOS) and the partial DOS for the $a(= c, f)$ orbital. These are defined as $\rho^{c+f}(E) = \rho^c(E) + \rho^f(E)$ and

$$\rho^a(E) = \frac{1}{2N} \sum_{p=1}^{2N} \left( \sum_{i=1}^{N} |\langle ia|\phi_p\rangle|^2 \right) \delta(E - E_p). \tag{12}$$

where $|\phi_p\rangle$ and $E_p$ represent the wave function and energy of the $p$th (single-particle) eigenstate of $\hat{H}_{\text{MF}}^{\text{total}}(t = 0)$, which are occupied in the ground state. $|ia\rangle$ is the wave function of an $a$-orbital electron at site $i$. Two sharp peaks in $\rho^{c+f}(E)$ originate from the existence of the macroscopic degenerate states (confined states) characteristic of the Penrose tiling [58,61]. When the system is in the BCS regime, the width between these two peaks is small, resulting in the large hybridization between $c$ and $f$ orbitals. In fact, the DOS at the gap edges is almost equally contributed by the partial DOSs for both orbitals. On the other hand, in the BEC case with $V = 4.28$, there are little overlap between $\rho^c$ and $\rho^f$, and thereby the DOS around the lower (higher) edge originates from the $f$ ($c$) orbitals. In the following, we discuss the photoinduced dynamics of the EI state in these two distinct regimes.

### B. Photoinduced dynamics

In our study, we examine the time evolution of the EI states in the BCS and BEC regimes to discuss the characteristic dynamics of the Penrose tiling. We focus on the cases with the interorbital interactions $V = 1.95$ and $4.28$ as examples of the BCS and BEC states. In these cases, the average of the order parameter is different from each other while the excitation gap takes the same value $\Delta_{\text{Gap}} = 0.2$, as shown in Fig. 2. We consider the photoinduced dynamics triggered by the single-cycle pulse with $\omega = 0.4$ and $t_p = 2\pi/\omega \simeq 15.7$ as in the previous study for the square lattice [48]. Here, we set the photon energy $\omega$ twice the excitation gap $\Delta_{\text{Gap}}$ so that it excites the quasiparticles with the energy beyond the gap.
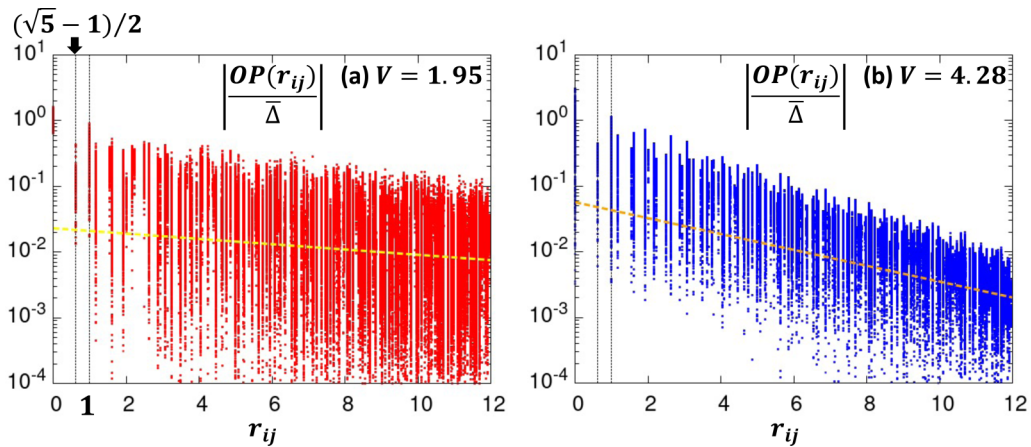


FIG. 3. Off-site electron-hole pair amplitude $OP(r_{ij})$ for the system with $N = 11\,006$ and $U = D = 4$ in (a) the BCS regime with $V = 1.95$ and in (b) the BEC regime with $V = 4.28$. Note that the shortest distance between two sites is the length of diagonal of skinny rhombus, whose length is $\frac{\sqrt{5}-1}{2}$. The yellow (orange) dashed line represents the slope of data set for $V = 1.95$ (4.28). These are obtained by using the least squares method for the data groups in $(r_{ij}, \log_{10}|OP/\overline{\Delta}|)$.
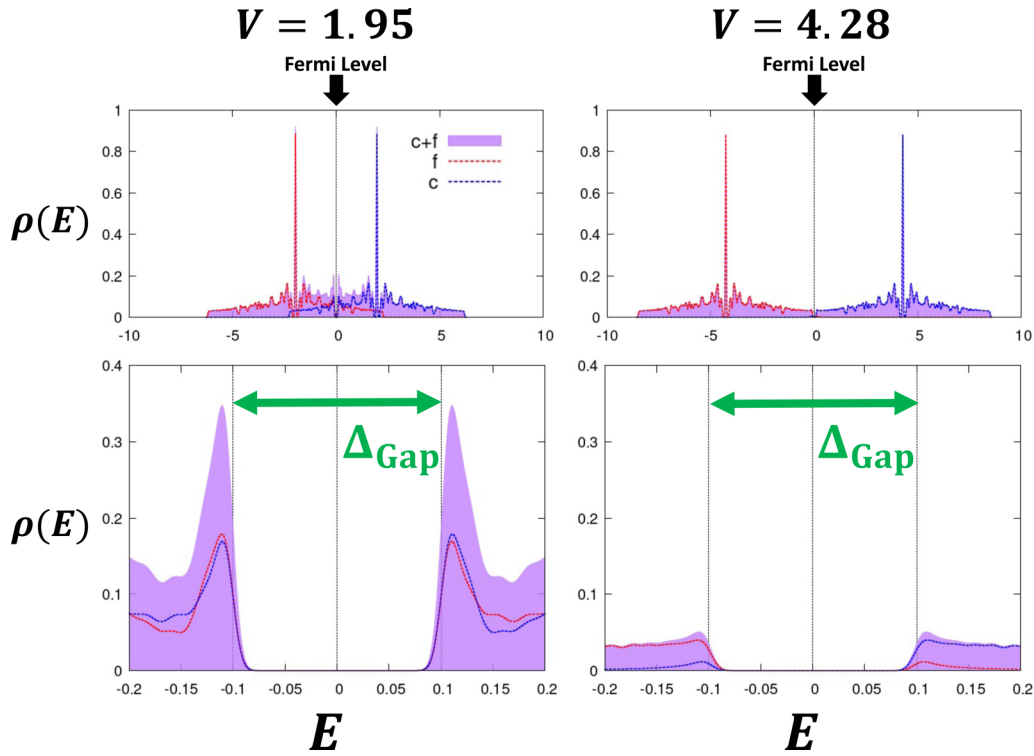
FIG. 4. The partial DOS $\rho^a(E)$ and the total DOS $\rho^{c+f}(E)$ in the system with $U = D = 4$ and $N = 11006$. Lower two figures show enlarged view of upper figures around the Fermi level ($E = 0$). Here, we approximate the Dirac delta function by the Gaussian function $\sqrt{1/\pi\sigma^2}e^{-x^2/\sigma^2}$ with a large value $\sigma^{-2}$ (small standard deviation). We use $\sigma^{-2} = 1000$ for upper figures and $\sigma^{-2} = 10\,000$ for lower figures. Note that the edges of the gaps are not sharp due to the Gaussian function used on behalf of the Dirac delta function.

In the following, we analyze the dynamics of physical quantities in three steps. Firstly, we focus on the spatial averaged quantities. Secondly, we discuss their coordination number dependence. Thirdly, we analyze physical quantities using the perpendicular space, which provides detailed information of their spatial pattern.

### 1. Spatial averaged values

Figure 5 shows the time evolution of bulk quantities $\overline{|\Delta(t)|} = \sum_{i=1}^{N} |\Delta_i(t)|/N$ and $\overline{n_c(t)} = \sum_{i=1}^{N} n_{ci}(t)/N$ in the system with $U = D = 4$. These quantities are modulated by the single-cycle pulse, and the behavior of the time evolution depends on the field strength $|F_0|$ and the interaction $V$. We find that no oscillation appears in the electron number for each orbital when $t > t_p$, as shown in Figs. 5(b) and 5(d). This is consistent with the constraint (11), as discussed above. By contrast, oscillatory behavior appears in the EI order parameter even when $t > t_p$, and the frequencies of the oscillations depend on the field strength, see Figs. 5(a) and 5(c). In the BCS regime with $V = 1.95$, the EI order parameter becomes smaller than the initial value $\overline{|\Delta(0)|}$. On the other hand, in the BEC regime, physical quantities behave differently from those in the BCS regime as shown in Figs. 5(c) and 5(d). In particular, the amplitude of the EI order parameter increases. Similar results, i.e., the increase (decrease) of the EI order parameter in the BEC (BCS) regime, have been obtained in the two-orbital Hubbard model on the square lattice [48]. In the BCS regime, the results may seem natural since electron-hole pairs are spatially extended and the detail lattice structure may

be less relevant for physical quantities. In the BEC regime, when $t = 0$, the $c$ orbital is almost empty and $f$ orbital is almost occupied. The introduction of the single-cycle pulse rapidly increases the electron number in the $c$ orbital, which leads to the formation of electron-hole pairs since the system remains coherent within the mean-field theory [50,51,71,72]. This picture is essentially the same as the explanation of the dynamics in the BEC region in the normal lattice [53], which is reduced to the dynamics of a two-level system.

### 2. Coordination number dependence

So far, we showed that the qualitative behavior of the spatially-averaged quantities is similar to that in normal crystals. We now focus on the spatial dependence of physical quantities and explore the effects of the quasiperiodic structure in the nonequilibrium dynamics. One of the important features of the Penrose tiling is that the coordination number at site $i$ $Z_i$ takes 3 to 7, in contrast to the square lattice with $Z_i = 4$. In the following, to avoid the boundary effects in the system, we consider the *bulk* region. The definition of it is explicitly shown in the Appendix B. The bulk region includes $N' = 7936$ sites when one treats the system with $N = 11\,006$. To see the coordination number dependence of physical quantities, we introduce the coordination-dependent averages as

$$|\Delta(t)|_\alpha = \frac{1}{N'_\alpha} \sum_{i \text{ with } Z_i=\alpha} |\Delta_i(t)|, \qquad (13)$$

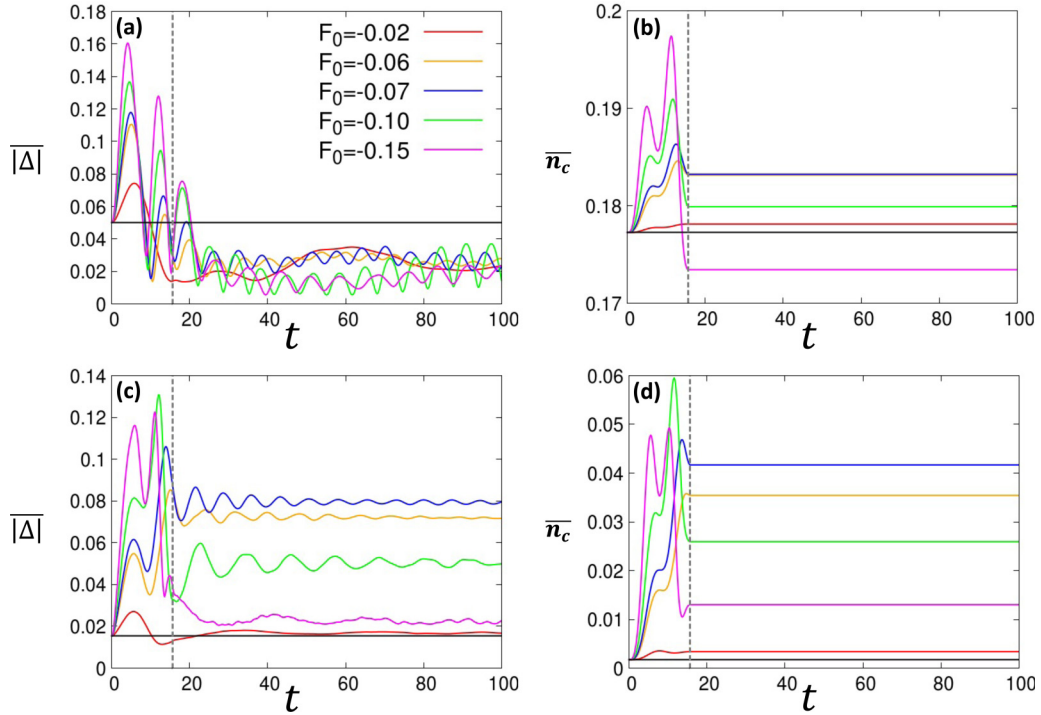$$n_c^\alpha(t) = \frac{1}{N'_\alpha} \sum_{i \text{ with } Z_i=\alpha} n_{ci}(t), \qquad (14)$$

FIG. 5. Time evolutions of $\overline{|\Delta|}$ and $\overline{n_c}$ in the system with $N = 11006$ and $U = D = 4$ after the single-cycle pulse is injected with several $F_0$. Upper panels are the results for the BCS case with $V = 1.95$, and lower ones are for the BEC case with $V = 4.28$. Horizontal-black lines indicate the initial values at $t = 0$ and vertical-dotted lines indicate $t_p$.

where $N'_\alpha$ is the number of the lattice sites with $Z_i = \alpha$ $(3, \cdots, 7)$ in the bulk region. Figure 6 shows the results for the system with $F_0 = -0.07$, around which the changes of $\overline{|\Delta|}$ and $\overline{n_c}$ are prominent as shown in Fig. 5. The standard deviations of the quantities are drawn as the shaded areas. We also plot averaged values $\overline{|\Delta(t)|}' = \sum_\alpha N'_\alpha |\Delta(t)|_\alpha / N'$ and $\overline{n_c(t)}' = \sum_\alpha N'_\alpha n_c^\alpha(t) / N'$. In the BCS regime, we found that all $|\Delta|_\alpha$ and $n_c^\alpha$ behave as $\overline{|\Delta|}'$ and $\overline{n_c}'$. Namely, the order parameters decreases and its oscillation frequency is independent of the coordination number, while the $c$-orbital electrons increase for all $\alpha$, as shown in Figs. 6(a) and 6(b). This similar behavior for the bulk averaged values may be reasonable since, in the BCS regime, electron-hole pairs are spatially extended and physical quantities should not strongly depend on the vertices. On the other hand, the coordination number dependence is different between $\overline{|\Delta|}'$ and $\overline{n_c}'$. We find that $n_c^\alpha$ is well classified by the coordination number, and $n_c^\alpha$ is larger for larger $\alpha$ both in and out of equilibrium. However, $|\Delta|_\alpha$ is not in accordance with the order of $\alpha$ and the dynamics of $|\Delta|_\alpha$ does not match with that of $n_c^\alpha$. This mismatch may reflects that, in the BCS regime, the electron-hole pairs are spatially extended and thus the excitonic properties are not determined only by local structures (vertices). In the BEC regime, we find that both $|\Delta|_\alpha$ and $n_c^\alpha$ increase from the initial values, and their dynamics is qualitatively similar to each other, see Figs. 6(c) and 6(d). Both $|\Delta|_\alpha$ and $n_c^\alpha$ are well classified by the coordination number $\alpha$, and they take larger value for larger $\alpha$. These behaviors should be attributed to that, in the BEC regime, the electron-hole pairs are tightly bounded and thus excitonic properties should be mainly determined by local structures (vertices). The match between

$|\Delta|_\alpha$ and $n_c^\alpha$ should be explained, by considering the atomic limit $J \to 0$ as Ref. [53]. In this limit, one can express the EI order $\phi$ by the electron number $n_c$ as $\sqrt{1 - (n_c - n_f)^2}/2$, which explains the similar behavior of $|\Delta|_\alpha$ and $n_c^\alpha$. However, we cannot see the clear dependence of the oscillation frequency of $|\Delta|_\alpha$ on the vertex type. The same thing happens with other $F_0$ in Fig. 5 (not shown). Figure 5(c) shows that the frequency of spatial averaged order parameter changes with $F_0$ values. The changes in frequency due to $F_0$ are phenomena, which are also observed in crystals [48]. Therefore, it is possible that the frequency depends more on the shape and intensity of external field than coordination numbers. The detailed analysis of the relation between the coordination number and frequency of EI order parameter is treated in the future work, and we do not discuss it further in this paper.

We now show that fluctuations of physical quantities can host characteristic behaviors in QCs. For example, oscillatory behavior appears in the electron number $n_c^\alpha$ at $t > t_p$ although their total number $\overline{n_c}$ is always constant. Such peculiar charge fluctuations have not been reported in the square lattice. Furthermore, these are not clearly visible in the BCS regime with $V = 1.95$. Since the change in $n_c$ induced by the photoirradiation is large in the BEC case, a charge oscillation is also large after the irradiation. Thus, we can say that charge fluctuations are inherent in the BEC regime. To look in detail the oscillatory behavior in $n_c^\alpha$ for the sites with $Z_i = \alpha$, we introduce the deviation from the time average as

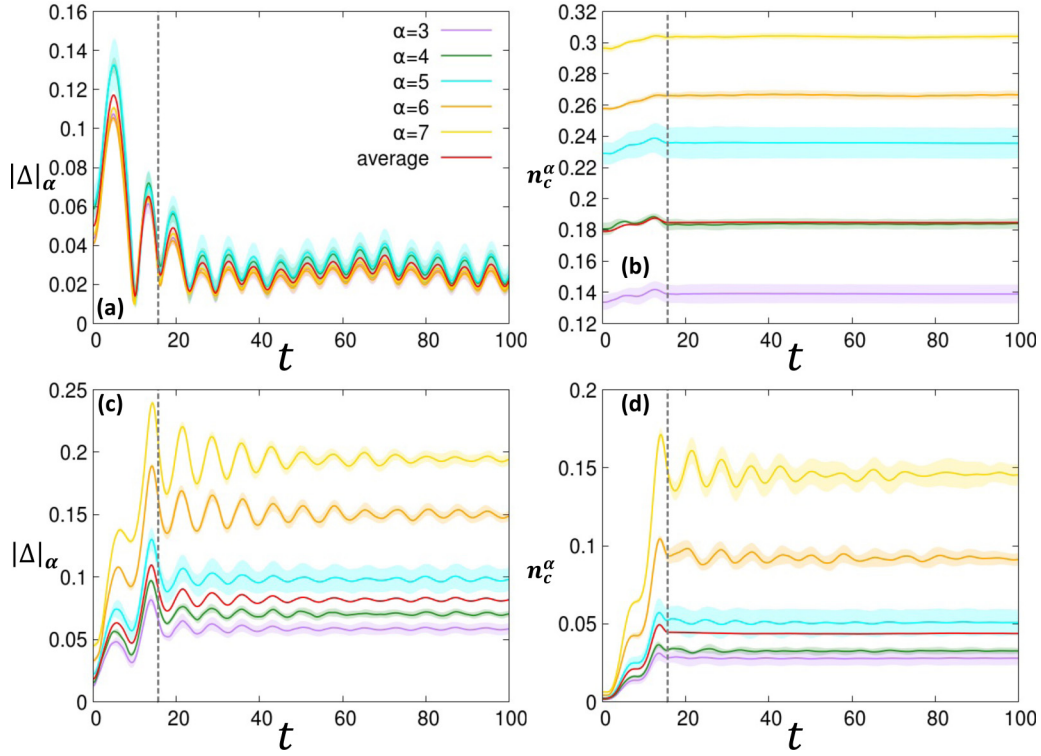$$\delta \widetilde{n_c^\alpha}(t) = \frac{n_c^\alpha(t)}{\widetilde{n_c}(\alpha)} - 1, \qquad (15)$$

FIG. 6. Photoinduced dynamics of $|\Delta|_\alpha$ and $n_c^\alpha$ for each $\alpha$ in the system after the single-cycle pulse is injected with $F_0 = -0.07$. Upper panels are the results for the BCS case with $V = 1.95$, and lower ones are for the BEC case with $V = 4.28$. Red lines represent $\overline{|\Delta|}'$ and $\overline{n_c}'$, and vertical-dotted lines represent $t_p$. Note that $\overline{n_c}'$ oscillates slightly although $\overline{n_c}$ is conserved when $t > t_p$, see Fig. 11 for an enlarged view of $\overline{n_c}'$.

where $\widetilde{n}_c(\alpha)(= \frac{1}{t_7 - t_1} \int_{t_1}^{t_7} n_c^\alpha(t) \, dt)$ is an average in the interval $(t_1, t_7)$, and $t_i$ is the maximum or minimum in the curve of $n_c^7(t)$ with $t > t_p$, see Fig. 7. We also plot $\delta\widetilde{n}_c'(t) = \overline{n_c}'(t)/\widetilde{n}_c' - 1$ where $\widetilde{n}_c'(= \frac{1}{t_7 - t_1} \int_{t_1}^{t_7} \overline{n_c}'(t) \, dt)$. The results are shown in Fig. 7. It is found that the charge oscillation induced by the single-cycle pulse decays with increasing $t$. The small
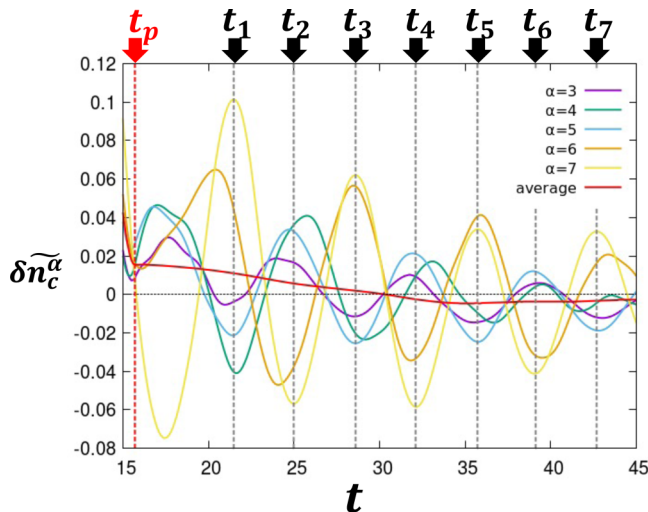
change of $\delta\widetilde{n}_c'$ $(\overline{n_c}')$ is caused by the finite size effect, see the Appendix C. We note that the quantities $n_c^\alpha$ can be classified into two groups $\{n_c^6, n_c^7\}$ and $\{n_c^3, n_c^4, n_c^5\}$, where the relative phase of their oscillations is almost $\pi$. This difference is consistent with the fact that the total number of electrons in $c$ orbital never changes when $t > t_p$. We note that the total number of electrons at each site $(n_{ci} + n_{fi})$ remains unity during the time evolution. Therefore, the charge oscillation is distinct from a charge density wave induced by the pulse.

### 3. Perpendicular space analysis

Now we discuss the site dependence of physical quantities from a bit different point of view using the perpendicular space [73]. This space is useful since it allows us to systematically discuss how the local lattice structures affect the physical quantities. On the Penrose tiling, each site is represented by the five-dimensional vector $\mathbf{n} = (n_1, n_2, n_3, n_4, n_5)$ with integers $n_\mu$ as shown in Fig. 1. Its coordinate $\boldsymbol{r}$ is constructed by the projection onto the two dimensions as

$$\boldsymbol{r} = (x, y) = (\mathbf{n} \cdot \mathbf{e}^x, \mathbf{n} \cdot \mathbf{e}^y), \tag{16}$$

where $e_\mu^x = \cos(\phi\mu + \theta_0)$, $e_\mu^y = \sin(\phi\mu + \theta_0)$, and $\phi = 2\pi/5$. The initial phase $\theta_0$ is arbitrary and we set $\theta_0 = -\frac{3\pi}{10}$ as an example. The projection onto the three-dimensional perpendicular space is given by

$$\tilde{\mathbf{r}} = (\tilde{x}, \tilde{y}) = (\mathbf{n} \cdot \tilde{\mathbf{e}}^x, \mathbf{n} \cdot \tilde{\mathbf{e}}^y), \tag{17}$$

$$\tilde{z} = \mathbf{n} \cdot \tilde{\mathbf{e}}^z, \tag{18}$$



FIG. 7. Photoinduced dynamics of $\delta\widetilde{n}_c^\alpha(t)$ for each $\alpha$ in the BEC case with $V = 4.28$ after the single-cycle pulse is injected with $F_0 = -0.07$. Red line represents $\delta\widetilde{n}_c'(t)$.
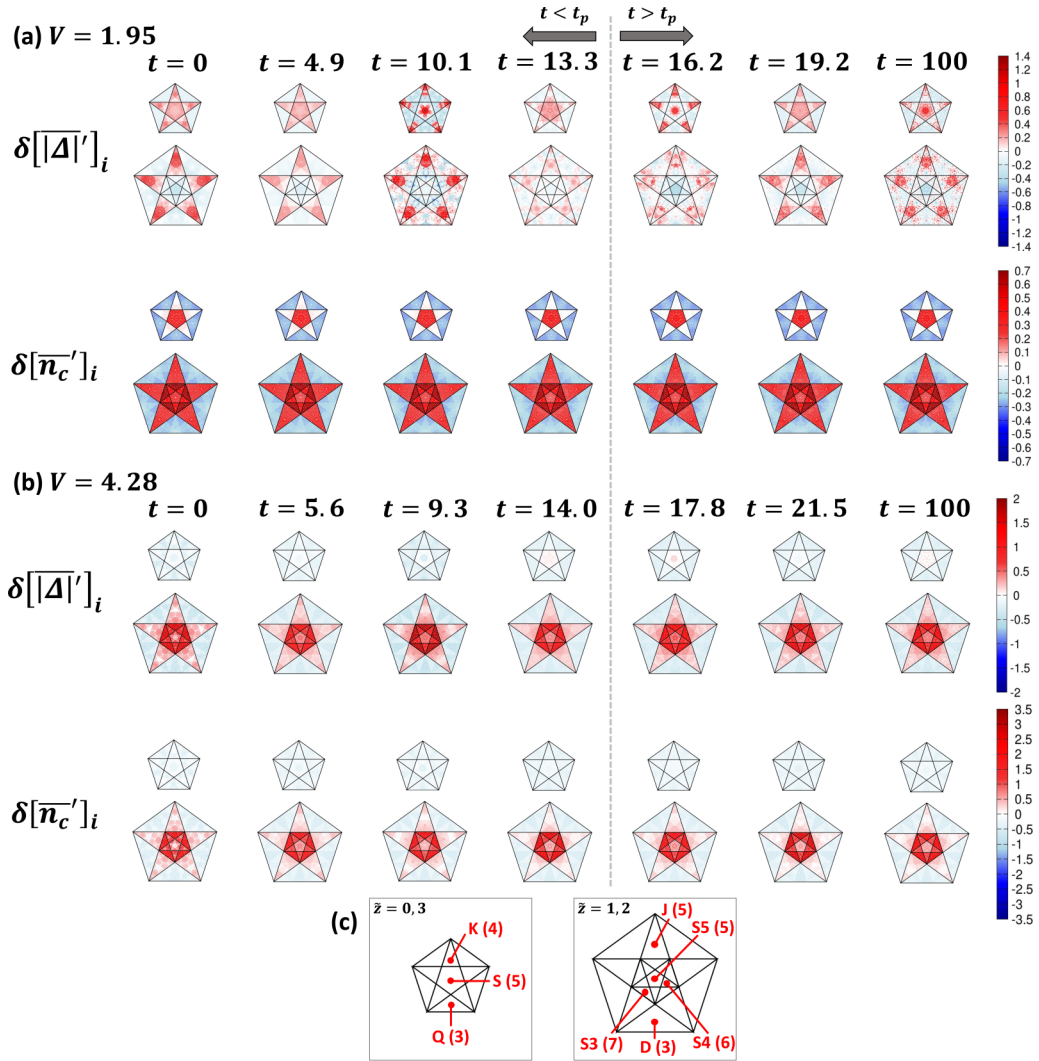
FIG. 8. Time-evolution of $\delta[\overline{|\Delta|}']_i$ and $\delta[\overline{n_c}']_i$ in the perpendicular space for the (a) BCS ($V = 1.95$) and (b) BEC ($V = 4.28$) cases with $F_0 = -0.07$. (c) Each domain is the region for the eight kinds of vertices shown in Fig. 1. The integer in parenthesis indicates the coordination number for each vertex.

where $\tilde{e}_\mu^x = \cos(2\phi\mu + \theta_0)$, $\tilde{e}_\mu^y = \sin(2\phi\mu + \theta_0)$, and $\tilde{e}_\mu^z = 1$. It is known that $\tilde{z}$ takes only four consecutive integers. In each $\tilde{z}$ plane, the $\tilde{\mathbf{r}}$ points densely cover a region of pentagon shape. The pentagon in $3 - \tilde{z}$ plane has the same size as the pentagon in $\tilde{z}$ plane. Eight kinds of vertices, which are quasiperiodically arranged in the real space as Fig. 1, are mapped to distinct domains, as shown in Fig. 8(c). Therefore, this perpendicular-space analysis allows us to discuss how site-dependent physical quantities are characterized by the local lattice structures, which include more information than the coordination number.

Here, we calculate the deviation of the quantities,

$$\delta[\overline{|\Delta|}']_i(t) = \frac{|\Delta_i(t)|}{\overline{|\Delta(t)|}} - 1, \qquad (19)$$

$$\delta[\overline{n_c}']_i(t) = \frac{n_{ci}(t)}{\overline{n_c(t)}} - 1, \qquad (20)$$

and we show the results in Fig. 8. Now, we plot $\delta[\overline{|\Delta|}']_i$ and $\delta[\overline{n_c}']_i$ on $\tilde{z}$ and $3 - \tilde{z}$ planes on the same plane because the

profiles for $\tilde{z}$ and $3 - \tilde{z}$ planes are identical in the thermodynamic limit ($N \to \infty$). When the system belongs to the BCS regime with $V = 1.95$, the average of $n_c^\alpha$ is little changed by the time evolution, as shown in Fig. 6(b). This is also found in the perpendicular space, where $\delta[\overline{n_c}']_i$ is almost constant in each domain for the corresponding vertex, as shown in Fig. 8(a). On the other hand, different behavior appears in the distribution of $|\Delta_i|$. In the initial state at $t = 0$, the pattern of $\delta[\overline{|\Delta|}']_i$ are different from that of $\delta[\overline{n_c}']_i$. Namely, the EI order parameter is not correlated with the local electron density. This means that the EI order parameters are not only determined by the local condition, which is consistent with that the electron-hole pairs are spatially extended in the BCS regime. After the single-cycle pulse is injected, the pattern of the order parameter is modified, while that of the electron number is hardly changed. For example, let us look at the $D$ and $J$ vertices. In the initial state, the magnitude of their order parameters is smaller (larger) than the total average on the the $D$ ($J$) vertices. However, at $t > 0$, we find red and blue regions in the $D$ and $J$ domains, which indicates the modulation of
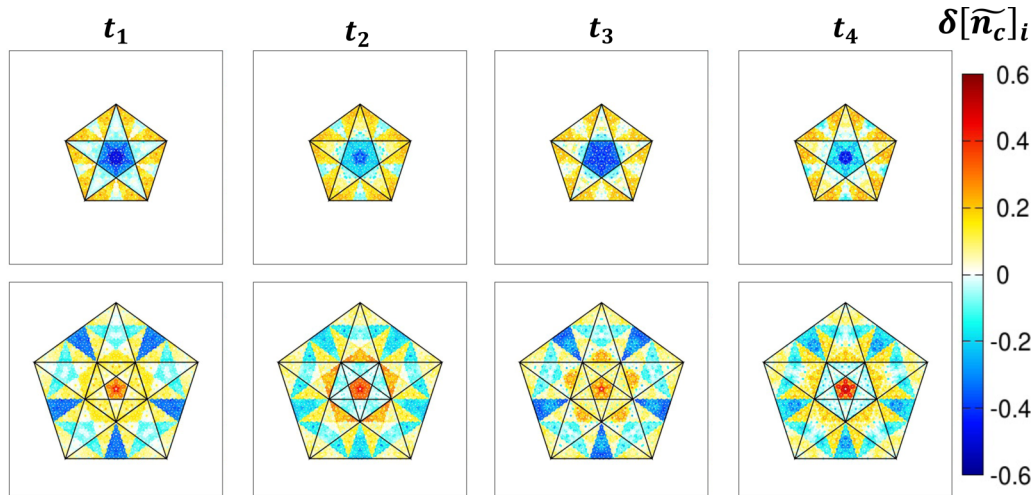
FIG. 9. Time-evolution of local charge fluctuations $\delta[\widetilde{n_c}]_i$ in the perpendicular space for the BEC case ($V = 4.28$) with $F_0 = -0.07$.

the spatial pattern even within these domains. By contrast, in the BEC case with $V = 4.28$, the pattern of $\delta[\overline{|\Delta|}']_i$ and $\delta[\overline{n_{c'}}']_i$ are similar in the perpendicular space, and it is hardly modified even after the excitation. This indicates that, in the BEC case, the system is mainly described only by the local lattice structures since electron-hole pairs are confined. We note that the mismatch (match) between the patterns of the EI order parameter and the $c$-orbital electron number in the BCS (BEC) regimes is consistent with the behavior previously reported in superconductivity on the Penrose tiling in equilibrium [62]. They found the mismatch (match) between the patterns of superconducting order parameter and electron number in the weak (strong) coupling regime. Our results newly show that the pattern of order parameter is sensitive against the excitation in the BCS regime, while it is insensitive in the BEC regime.

Finally, we analyze the charge fluctuations using the perpendicular space. To see the spatial pattern of the charge fluctuations, we show $\delta[\widetilde{n}_c]_i(t) = n_{ci}(t)/\widetilde{n}_c(Z_i) - 1$ for the BEC state ($V = 4.28$) with $F_0 = -0.07$ in Fig. 9. In the domains for $S4$ and $S3$ vertices where $\alpha = 6, 7$ in the perpendicular space, we find that the quantities clearly oscillate together with sign changes. By contrast, in the other domains for $\alpha = 3, 4$, and $5$, we could not see clear oscillatory behavior with sign changes. In addition, we find that the domain can be further classified into some subdomains. For examples, the $D$ domain is split into seven subdomains, as shown in Fig. 9. These two points are consistent with the fact that the width of oscillations is smaller than its standard deviation, as shown in Fig. 6(d). The existence of subdomain structures implies that the local charge fluctuations are affected by not only the coordination number but also the environment of the connecting sites. In fact, such a subdomain structure in $\delta[\widetilde{n}_c]_i$ is not changed during the time evolution.

We wish to note that even when the initial state is in the band insulating state with $\Delta_i = 0$ and $V > V_c$, substantial size of the excitonic order parameter appears due to the single-cycle pulse and oscillatory behavior similar to the BEC regime emerges (reported in Ref. [74]). This implies the existence of photoinduced transient EI order [72] in the QC,

and our results may be relevant for dynamics of photoexcited semiconductors. Although neither of an excitonic insulator or a semiconductor on a QC has been found up to now, the semiconducting approximant Al-Si-Ru has recently been synthesized [4]. We believe that semiconducting QC will be synthesized in near future, and interesting excitonic properties discussed here should be observed.

## IV. SUMMARY AND OUTLOOK

In this study, we have examined the photoinduced dynamics of the EI phase in the two-orbital Hubbard model on the Penrose tiling. We have shown that the dynamics is qualitatively similar to that in the square lattice as far as we focus on the bulk quantities. Namely, it is found that after the single-cycle pulse is injected the magnitude of the EI order parameters decreases in the BCS regime and it increases in the BEC regime. Furthermore, we have demonstrated that spatial dependence of physical quantities and their fluctuations show characteristic behaviors in the Penrose tiling. Examining the coordination number dependence in the physical quantities, we have found oscillatory behavior of the $c$-orbital electron number. Since the charge oscillation is not prominent in the BCS regime, the induced charge fluctuations are inherent in the BEC regime. We further clarified the difference of the dynamics between the BCS and BEC regimes in terms of the perpendicular space analysis. In the BEC regime, the patterns of the EI order parameter and the number of $c$-orbital electron are similar, which holds even after the photoexcitation. On the other hand, in the BCS regime, the pattern of the EI order parameter is distinct from that of the $c$-orbital electron number. In particular, the pattern of the order parameters changes remarkably with the photoexcitation.

In our study, we showed that the rich local structures involved in QCs can lead to interesting nonequilibrium dynamics of physical quantities. Still, to be strict, we have to note that the similar spatial dependence may be also observed in the normal crystals with multiple coordination numbers or approximants. In order to rigorously identify the unique features in QCs, further systematic comparison with various
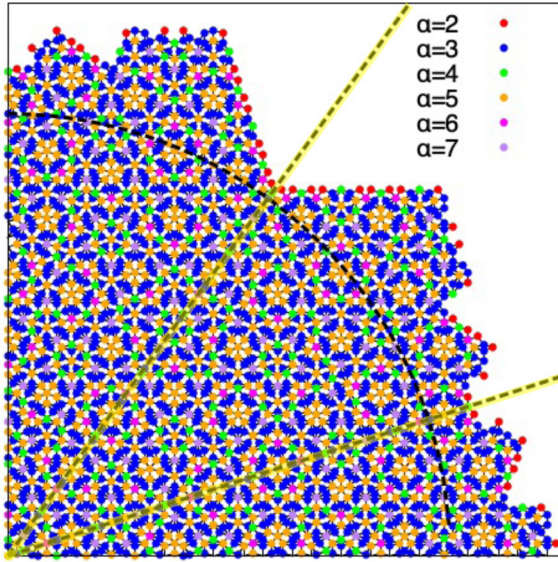
FIG. 10. The area within the dashed arc line indicates the bulk region. The area between two yellow lines in the figure is one of the ten equivalent regions defined by the $C_{5v}$ symmetry of the Penrose tiling.

types of lattice may be needed. For such exploration, the detailed analysis of the patterns in the perpendicular space should be useful.

We also wish to comment on the experimental realization of the EI state in QCs. Although we have studied the EI state in the theoretically ideal situation, in real materials the existence of the EI state and how to distinguish this state from other ordered states are still controversial even in normal crystals [40,41,43,45,70,75–88]. Thus, the direct experimental observation of the characteristic EI dynamics discussed in this paper may be difficult. Still we believe that the photoinduced nonequilibrium dynamics in quasicrystalline systems hosts potentially interesting questions and our work should be a milestone for researches in this direction. We expect that characteristic spatial-dependent dynamics can also be observed in various ordered phase, such as the superconducting phase and the antiferromagnetic phase, in the QC. The perpendicular space analysis should be useful also in these cases as we demonstrated here. One of interesting topics in the field is the role of the confined states, which are macroscopically degenerate states peculiar to quasicrystals. In our previous paper [58], it has been found that the EI order parameter shows intriguing spatial distribution reflecting the confined states. It is interesting and important to clarify that this unique distribution can be photoinduced or changed in response to the photoirradiation. These are now under consideration.

## ACKNOWLEDGMENTS

## APPENDIX A: DERIVATION OF MF HAMILTONIAN

We derive the MF Hamiltonian (6) from the full Hamiltonian $\hat{H}^{\text{total}}(t) = \hat{H} + \hat{H}_{\text{ex}}(t)$, which consists of Eqs. (1) and (2). Applying the Hartree-Fock decoupling to the interaction term at each site in the full Hamiltonian, we first obtain the MF Hamiltonian $\hat{H}_{\text{MF}}^{\text{total}}$ as

$$
\begin{aligned}
\hat{H}_{\text{MF}}^{\text{total}}(t) = {} & -J \sum_{\langle i,j \rangle \sigma} (\hat{c}_{i\sigma}^{\dagger} \hat{c}_{j\sigma} - \hat{f}_{i\sigma}^{\dagger} \hat{f}_{j\sigma}) + \frac{D}{2} \sum_{i\sigma} (\hat{n}_{ci\sigma} - \hat{n}_{fi\sigma}) \\
& - \mu \sum_{i\sigma} (\hat{n}_{fi\sigma} + \hat{n}_{ci\sigma}) \\
& + U \sum_{i\sigma} (n_{ci}(t)\hat{n}_{ci\sigma} + n_{fi}(t)\hat{n}_{fi\sigma}) \\
& + 2V \sum_{i\sigma} (n_{fi}(t)\hat{n}_{ci\sigma} + n_{ci}(t)\hat{n}_{fi\sigma}) \\
& - \sum_{i\sigma} [\{V \Delta_i(t) - F_{\text{ex}}(t)\}\hat{f}_{i\sigma}^{\dagger} \hat{c}_{i\sigma} + \text{H.c.}].
\end{aligned} \quad \text{(A1)}
$$

The Hartree and chemical potential terms,

$$
\sum_{i\sigma} [\{U n_{ci}(t) + 2V n_{fi}(t) - \mu\}\hat{n}_{ci\sigma} \\
+ \{U n_{fi}(t) + 2V n_{ci}(t) - \mu\}\hat{n}_{fi\sigma}], \quad \text{(A2)}
$$

can be simplified by the half-filling condition, i.e., $\mu = U/2 + V$, $n_{ci}(t) + n_{fi}(t) = 1$. Namely, under this condition, the term is expressed as

$$
(2V - U) \sum_{i\sigma} \left[ \left\{ n_{ci}(t) - \frac{1}{2} \right\} \hat{n}_{fi\sigma} + \left\{ n_{fi}(t) - \frac{1}{2} \right\} \hat{n}_{ci\sigma} \right]. \quad \text{(A3)}
$$

Finally, we omit the spin index and obtain Eq. (6).

## APPENDIX B: BULK REGION IN OUR MODEL

In order to eliminates the effects of the edges, we define the *bulk* region as an area within a reasonable distance from the center of the tiling. Specifically, we take a circular area as shown in Fig. 10. The system has the $C_{5v}$ symmetry and it can be separated into ten equivalent regions, one of which is the area between two yellow lines in Fig. 10. The area inside the black dashed arc is taken as the bulk region in the $N = 11006$ system we used. When we denote the number of sites with the coordination number $\alpha$ in the whole system and in the bulk region as $N_\alpha$ and $N'_\alpha$, respectively, we have $(N_2, N_3, N_4, N_5, N_6, N_7) = (180, 5795, 995, 3066, 405, 565)$ and $(N'_2, N'_3, N'_4, N'_5, N'_6, N'_7) = (0, 4195, 725, 2296, 275, 445)$.
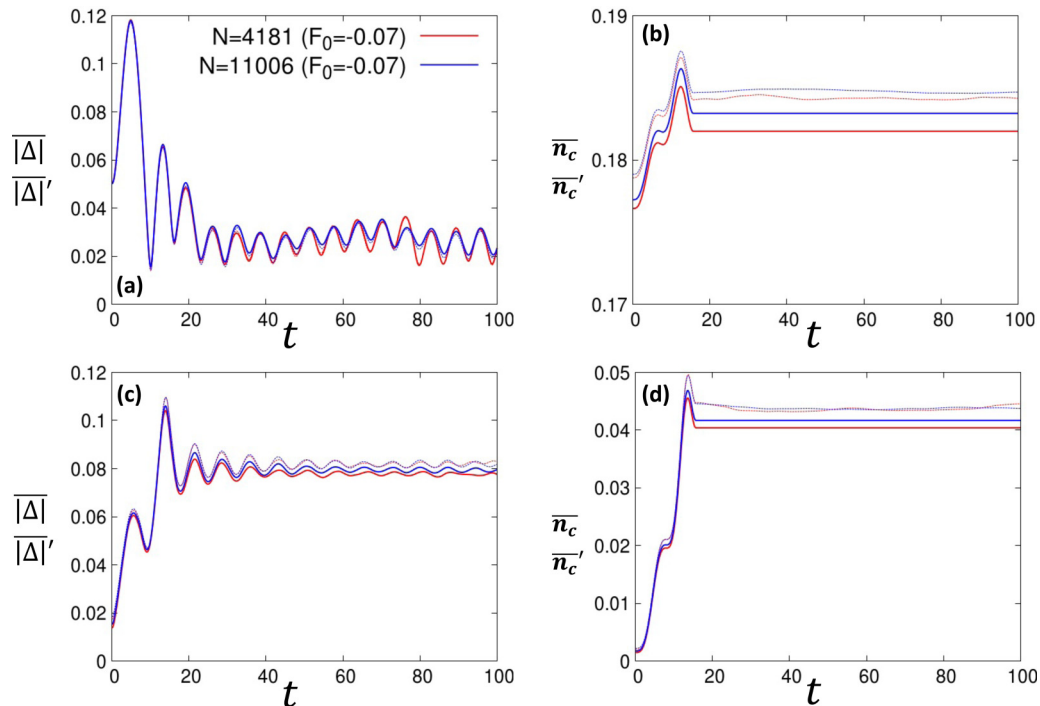
FIG. 11. Comparison of photoinduced dynamics between the system with $N = 11\,006$ and the system with $N = 4181$ under the condition $(U, D, \omega, F_0) = (4, 4, 0.4, -0.07)$. [(a), (b)] Time evolution of $\overline{|\Delta|}$ and $\overline{n_c}$ for $V = 1.95$. [(c), (d)] Time evolution of $\overline{|\Delta|}$ and $\overline{n_c}$ for $V = 4.28$. Dashed lines represent $\overline{|\Delta|}'$ and $\overline{n_c}'$ for each system.

## APPENDIX C: THE EFFECTS OF THE SYSTEM SIZE AND EDGES

To discuss the effects of the system size and edges, we look at the dynamics of $\overline{|\Delta|}$, $\overline{|\Delta|}'$, $\overline{n_c}$, and $\overline{n_c}'$ under the conditions, $(U, D, V, \omega, F_0) = (4, 4, 1.95, 0.4, -0.07)$ and $(U, D, V, \omega, F_0) = (4, 4, 4.28, 0.4, -0.07)$, in the system with $N = 11\,006$ ($N' = 7936$) and the system with $N = 4181$ ($N' = 2921$), see Fig. 11. It is found that the qualitative behavior of $\overline{|\Delta|}$, $\overline{|\Delta|}'$, $\overline{n_c}$, and $\overline{n_c}'$ is similar in the systems with $N = 11\,006$ and $N = 4181$. However, strictly speaking, the detailed values of $\overline{|\Delta|}$, $\overline{|\Delta|}'$, $\overline{n_c}$, and $\overline{n_c}'$ are different. If we want to evaluate the accurate values in the thermodynamic limit, we need to calculate the time evolution for larger systems, which is too expensive for the current computational resources. Therefore, in this paper, we focus on the qualitative aspects.

[1] D. Shechtman, I. Blech, D. Gratias, and J. W. Cahn, Phys. Rev. Lett. **53**, 1951 (1984).

[2] D. Levine and P. J. Steinhardt, Phys. Rev. Lett. **53**, 2477 (1984).

[3] K. Kamiya, T. Takeuchi, N. Kabeya, N. Wada, T. Ishimasa, A. Ochiai, K. Deguchi, K. Imura, and N. Sato, Nat. Commun. **9**, 154 (2018).

[4] Y. Iwasaki, K. Kitahara, and K. Kimura, Phys. Rev. Materials **3**, 061601(R) (2019).

[5] K. Kimura, H. Iwahashi, T. Hashimoto, S. Takeuchi, U. Mizutani, S. Ohashi, and G. Itoh, J. Phys. Soc. Jpn. **58**, 2472 (1989).

[6] B. D. Biggs, S. J. Poon, and N. R. Munirathnam, Phys. Rev. Lett. **65**, 2700 (1990).

[7] T. Klein, C. Berger, D. Mayou, and F. Cyrot-Lackmann, Phys. Rev. Lett. **66**, 2907 (1991).

[8] S. J. Poon, Adv. Phys. **41**, 303 (1992).

[9] H. Akiyama, Y. Honda, T. Hashimoto, K. Edagawa, and S. Takeuchi, Jpn. J. Appl. Phys. **32**, L1003 (1993).

[10] K. Edagawa and K. Kajiyama, Mater. Sci. Eng. A **294-296**, 646 (2000).

[11] K. Edagawa, K. Kajiyama, R. Tamura, and S. Takeuchi, Mater. Sci. Eng. A **312**, 293 (2001).

[12] A. Inaba, R. Lortz, C. Meingast, J. Guo, and A.-P. Tsai, J. Alloys Compd. **342**, 302 (2002).

[13] A. F. Prekul, V. A. Kazantsev, N. I. Shchegolikhina, R. I. Gulyaeva, and K. Edagawa, Phys. Solid State **50**, 2013 (2008).

[14] S. Tamura, K. Fukushima, Y. Tokumoto, Y. Takagiwa, and K. Edagawa, Mater. Trans. **62**, 356 (2021).

[15] F. Iglói, G. Roósz, and Y.-C. Lin, New J. Phys. **15**, 023036 (2013).

[16] M. A. Bandres, M. C. Rechtsman, and M. Segev, Phys. Rev. X **6**, 011016 (2016).

[17] K. Yonemitsu and K. Nasu, Phys. Rep. **465**, 1 (2008).

[18] H. Aoki, N. Tsuji, M. Eckstein, M. Kollar, T. Oka, and P. Werner, Rev. Mod. Phys. **86**, 779 (2014).

[19] C. Giannetti, M. Capone, D. Fausti, M. Fabrizio, F. Parmigiani, and D. Mihailovic, Adv. Phys. **65**, 58 (2016).

[20] D. N. Basov, R. D. Averitt, and D. Hsieh, Nat. Mater. **16**, 1077 (2017).

[21] A. Cavalleri, Contemp. Phys. **59**, 31 (2018).

[22] T. Oka and S. Kitamura, Annu. Rev. Condens. Matter Phys. **10**, 387 (2019).

[23] A. de la Torre, D. M. Kennes, M. Claassen, S. Gerber, J. W. McIver, and M. A. Sentef, Rev. Mod. Phys. **93**, 041002 (2021).

[24] D. Fausti, R. I. Tobey, N. Dean, S. Kaiser, A. Dienst, M. C. Hoffmann, S. Pyon, T. Takayama, H. Takagi, and A. Cavalleri, Science **331**, 189 (2011).

[25] S. Kaiser, C. R. Hunt, D. Nicoletti, W. Hu, I. Gierz, H. Y. Liu, M. Le Tacon, T. Loew, D. Haug, B. Keimer, and A. Cavalleri, Phys. Rev. B **89**, 184516 (2014).

[26] M. Mitrano, A. Cantaluppi, D. Nicoletti, S. Kaiser, A. Perucchi, S. Lupi, P. Di Pietro, D. Pontiroli, M. Riccò, S. R. Clark, D. Jaksch, and A. Cavalleri, Nature (London) **530**, 461 (2016).

[27] T. Suzuki, T. Someya, T. Hashimoto, S. Michimae, M. Watanabe, M. Fujisawa, T. Kanai, N. Ishii, J. Itatani, S. Kasahara, Y. Matsuda, T. Shibauchi, K. Okazaki, and S. Shin, Commun. Phys. **2**, 115 (2019).

[28] L. Stojchevska, I. Vaskivskyi, T. Mertelj, P. Kusar, D. Svetin, S. Brazovskii, and D. Mihailovic, Science **344**, 177 (2014).

[29] M. Porer, U. Leierseder, J.-M. Ménard, H. Dachraoui, L. Mouchliadis, I. E. Perakis, U. Heinzmann, J. Demsar, K. Rossnagel, and R. Huber, Nat. Mater. **13**, 857 (2014).

[30] T. Ishikawa, Y. Sagae, Y. Naitoh, Y. Kawakami, H. Itoh, K. Yamamoto, K. Yakushi, H. Kishida, T. Sasaki, S. Ishihara, Y. Tanaka, K. Yonemitsu, and S. Iwai, Nat. Commun. **5**, 5528 (2014).

[31] A. Kogar, A. Zong, P. E. Dolgirev, X. Shen, J. Straquadine, Y.-Q. Bie, X. Wang, T. Rohwer, I.-C. Tung, Y. Yang *et al.*, Nat. Phys. **16**, 159 (2020).

[32] F. Zhou, J. Williams, S. Sun, C. D. Malliakas, M. G. Kanatzidis, A. F. Kemper, and C.-Y. Ruan, Nat. Commun. **12**, 566 (2021).

[33] M. Trigo, P. Giraldo-Gallo, J. N. Clark, M. E. Kozina, T. Henighan, M. P. Jiang, M. Chollet, I. R. Fisher, J. M. Glownia, T. Katayama, P. S. Kirchmann, D. Leuenberger, H. Liu, D. A. Reis, Z. X. Shen, and D. Zhu, Phys. Rev. B **103**, 054109 (2021).

[34] L. V. Keldish and Y. V. Kopaev, Sov. Phys. Solid State **6**, 2219 (1965).

[35] D. Jérome, T. M. Rice, and W. Kohn, Phys. Rev. **158**, 462 (1967).

[36] Y. Wakisaka, T. Sudayama, K. Takubo, T. Mizokawa, M. Arita, H. Namatame, M. Taniguchi, N. Katayama, M. Nohara, and H. Takagi, Phys. Rev. Lett. **103**, 026402 (2009).

[37] Y. Wakisaka, T. Sudayama, K. Takubo, T. Mizokawa, N. L. Saini, M. Arita, H. Namatame, M. Taniguchi, N. Katayama, M. Nohara, and H. Takagi, J. Supercond. Novel Magn. **25**, 1231 (2012).

[38] H. Cercellier, C. Monney, F. Clerc, C. Battaglia, L. Despont, M. G. Garnier, H. Beck, P. Aebi, L. Patthey, H. Berger, and L. Forró, Phys. Rev. Lett. **99**, 146403 (2007).

[39] C. Monney, C. Battaglia, H. Cercellier, P. Aebi, and H. Beck, Phys. Rev. Lett. **106**, 106404 (2011).

[40] S. Mor, M. Herzog, D. Golež, P. Werner, M. Eckstein, N. Katayama, M. Nohara, H. Takagi, T. Mizokawa, C. Monney, and J. Stähler, Phys. Rev. Lett. **119**, 086401 (2017).

[41] E. Baldini, A. Zong, D. Choi, C. Lee, M. H. Michael, L. Windgaetter, I. I. Mazin, S. Latini, D. Azoury, B. Lv *et al.*, arXiv:2007.02909.

[42] S. Hellmann, T. Rohwer, M. Kalläne, K. Hanff, C. Sohrt, A. Stange, A. Carr, M. M. Murnane, H. C. Kapteyn, L. Kipp, M. Bauer, and K. Rossnagel, Nat. Commun. **3**, 1069 (2012).

[43] K. Okazaki, Y. Ogawa, T. Suzuki, T. Yamamoto, T. Someya, S. Michimae, M. Watanabe, Y. Lu, M. Nohara, H. Takagi *et al.*, Nat. Commun. **9**, 4322 (2018).

[44] T. Mitsuoka, T. Suzuki, H. Takagi, N. Katayama, H. Sawa, M. Nohara, M. Watanabe, J. Xu, Q. Ren, M. Fujisawa *et al.*, J. Phys. Soc. Jpn. **89**, 124703 (2020).

[45] T. Saha, D. Golež, G. De Ninno, J. Mravlje, Y. Murakami, B. Ressel, M. Stupar, and P. c. v. R. Ribič, Phys. Rev. B **103**, 144304 (2021).

[46] D. Golež, P. Werner, and M. Eckstein, Phys. Rev. B **94**, 035121 (2016).

[47] Y. Murakami, D. Golež, M. Eckstein, and P. Werner, Phys. Rev. Lett. **119**, 247601 (2017).

[48] Y. Tanaka, M. Daira, and K. Yonemitsu, Phys. Rev. B **97**, 115105 (2018).

[49] T. Tanabe, K. Sugimoto, and Y. Ohta, Phys. Rev. B **98**, 235127 (2018).

[50] E. Perfetto, D. Sangalli, A. Marini, and G. Stefanucci, Phys. Rev. Materials **3**, 124601 (2019).

[51] Y. Murakami, M. Schüler, S. Takayoshi, and P. Werner, Phys. Rev. B **101**, 035203 (2020).

[52] Y. Murakami, D. Golež, T. Kaneko, A. Koga, A. J. Millis, and P. Werner, Phys. Rev. B **101**, 195118 (2020).

[53] Y. Tanaka and K. Yonemitsu, Phys. Rev. B **102**, 075118 (2020).

[54] E. Perfetto and G. Stefanucci, Phys. Rev. Lett. **125**, 106401 (2020).

[55] P. Werner and Y. Murakami, Phys. Rev. B **102**, 241103(R) (2020).

[56] R. Tuovinen, D. Golež, M. Eckstein, and M. A. Sentef, Phys. Rev. B **102**, 115157 (2020).

[57] R. Penrose, Bull. Inst. Math. Appl. **10**, 266 (1974).

[58] K. Inayoshi, Y. Murakami, and A. Koga, J. Phys. Soc. Jpn. **89**, 064002 (2020).

[59] N. de Bruijn, Indaga. Math. **84**, 39 (1981).

[60] N. de Bruijn, Indag. Math. **84**, 53 (1981).

[61] M. Arai, T. Tokihiro, T. Fujiwara, and M. Kohmoto, Phys. Rev. B **38**, 1621 (1988).

[62] S. Sakai, N. Takemori, A. Koga, and R. Arita, Phys. Rev. B **95**, 024509 (2017).

[63] A. Koga and H. Tsunetsugu, Phys. Rev. B **96**, 214402 (2017).

[64] S. Sakai and R. Arita, Phys. Rev. Research **1**, 022002(R) (2019).

[65] N. Takemori, R. Arita, and S. Sakai, Phys. Rev. B **102**, 115108 (2020).

[66] A. Koga, Phys. Rev. B **102**, 115125 (2020).

[67] N. Tsuji, M. Eckstein, and P. Werner, Phys. Rev. Lett. **110**, 136404 (2013).

[68] J. Kuneš and P. Augustinský, Phys. Rev. B **89**, 115134 (2014).

[69] J. Kuneš, J. Phys.: Condens. Matter **27**, 333201 (2015).

[70] G. Mazza, M. Rösner, L. Windgätter, S. Latini, H. Hübener, A. J. Millis, A. Rubio, and A. Georges, Phys. Rev. Lett. **124**, 197601 (2020).

[71] T. Östreich and K. Schönhammer, Z. Phys. B **91**, 189 (1993).

[72] Y. Murotani, C. Kim, H. Akiyama, L. N. Pfeiffer, K. W. West, and R. Shimano, Phys. Rev. Lett. **123**, 197401 (2019).

[73] P. J. Steinhardt and S. Ostlund, *The Physics of Quasicrystals* (World Scientific, Singapore, 1987).

[74] K. Inayoshi, Y. Muarkami, and A. Koga, J. Phys.: Conf. Ser. **2164**, 012050 (2022).

[75] T. Kaneko, T. Toriyama, T. Konishi, and Y. Ohta, Phys. Rev. B **87**, 035121 (2013).

[76] B. Zenker, H. Fehske, and H. Beck, Phys. Rev. B **90**, 195118 (2014).

[77] K. Sugimoto, T. Kaneko, and Y. Ohta, Phys. Rev. B **93**, 041105(R) (2016).

[78] Y. F. Lu, H. Kono, T. I. Larkin, A. W. Rost, T. Takayama, A. V. Boris, B. Keimer, and H. Takagi, Nat. Commun. **8**, 14408 (2017).

[79] T. I. Larkin, A. N. Yaresko, D. Pröpper, K. A. Kikoin, Y. F. Lu, T. Takayama, Y.-L. Mathis, A. W. Rost, H. Takagi, B. Keimer, and A. V. Boris, Phys. Rev. B **95**, 195144 (2017).

[80] A. Kogar, M. S. Rak, S. Vig, A. A. Husain, F. Flicker, Y. I. Joe, L. Venema, G. J. MacDougall, T. C. Chiang, E. Fradkin, J. van Wezel, and P. Abbamonte, Science **358**, 1314 (2017).

[81] M. D. Watson, I. Marković, E. A. Morales, P. Le Fèvre, M. Merz, A. A. Haghighirad, and P. D. C. King, Phys. Rev. Research **2**, 013236 (2020).

[82] T. Tang, H. Wang, S. Duan, Y. Yang, C. Huang, Y. Guo, D. Qian, and W. Zhang, Phys. Rev. B **101**, 235148 (2020).

[83] A. Subedi, Phys. Rev. Materials **4**, 083601 (2020).

[84] M.-J. Kim, A. Schulz, T. Takayama, M. Isobe, H. Takagi, and S. Kaiser, Phys. Rev. Research **2**, 042039(R) (2020).

[85] K. Kim, H. Kim, J. Kim, C. Kwon, J. S. Kim, and B. J. Kim, Nat. Commun. **12**, 1969 (2021).

[86] P. A. Volkov, M. Ye, H. Lohani, I. Feldman, A. Kanigel, and G. Blumberg, npj Quantum Mater. **6**, 52 (2021).

[87] H. M. Bretscher, P. Andrich, Y. Murakami, D. Golež, B. Remez, P. Telang, A. Singh, L. Harnagea, N. R. Cooper, A. J. Millis *et al.*, Sci. Adv. **7**, eabd6147 (2021).

[88] T. Miyamoto, M. Mizui, N. Takamura, J. Hirata, H. Yamakawa, T. Morimoto, T. Terashige, N. Kida, A. Nakano, H. Sawa, and H. Okamoto, J. Phys. Soc. Jpn. **91**, 023701 (2022).